SCIENCE CHINA
Chemistry

•ARTICLES•

November 2018 Vol.61 No.11: 1413–1422
https://doi.org/10.1007/s11426-018-9284-4

BODIPY-derived ratiometric fluorescent sensors: pH-regulated aggregation-induced emission and imaging application in cellular acidification triggered by crystalline silica exposure

Yang Bai, Danyang Liu, Zhong Han, Yuncong Chen, Zhongyan Chen, Yang Jiao, Weijiang He* & Zijian Guo*

State Key Laboratory of Coordination Chemistry, Coordination Chemistry Institute, School of Chemistry and Chemical Engineering, Nanjing University, Nanjing 210023, China

Received April 7, 2018; accepted May 15, 2018; published online July 23, 2018

Modification of classic fluorophore to possess the emission transitions between aggregation-induced emission (AIE) and intrinsic emission offers reliable approach to the design of ratiometric fluorescent sensors. In this study, a proton acceptor benzimidazole was integrated with BODIPY to form three compounds, **BBI-1/2/3**, which demonstrated the AIE (~595 nm, I_{agg}) in neutral aqueous medium and intrinsic BODIPY emission (~510 nm, I_{int}) in acidic medium. All the three showed the ratiometric pH sensing behavior in a dual excitation/dual emission mode, yet BBI-3 displayed still the dual emission ratiometric pH sensing ability. The pH-dependent emission ratio I_{int}/I_{agg} of the three were fully reversible, and no interference was observed from normal abundant chemical species in live cells. Their different pK_a (**BBI-1**, pK_a 4.4; **BBI-2**, pK_a 2.7; **BBI-3**, pK_a 3.6) suggested that the substituents on benzimidazole moiety were essential to govern their functioning pH range. The ratiometric imaging of **BBI-1** in A549 cells provided an effective intracellular pH (pH_i) calibration formula corresponding to emission ratio of I_{int}/I_{agg}. Ratiometric pH_i imaging in A549 cells upon small particle exposure confirmed the particle-induced cellular acidification with this formula. Both particle size and the chemical nature of the particle contribute to the observed acidification effect. The synchronization of lysosome disruption to cellular acidification in A549 cells upon crystalline silica exposure was directly observed for the first time with **BBI-1**, showing the potential application of **BBI-1** in the study of silicosis and other related diseases. This study demonstrated that endowing fluorophore with AIE/intrinsic emission transition could be a promising strategy for ratiometric sensor design.

fluorescence imaging, sensor, cellular acidification, aggregation-induced emission, crystalline silica, lysosome, BODIPY

Citation: Bai Y, Liu D, Han Z, Chen Y, Chen Z, Jiao Y, He W, Guo Z. BODIPY-derived ratiometric fluorescent sensors: pH-regulated aggregation-induced emission and imaging application in cellular acidification triggered by crystalline silica exposure. *Sci China Chem*, 2018, 61: 1413–1422, https://doi.org/10.1007/s11426-018-9284-4

1 Introduction

Intracellular pH (pH_i) is one of the key microenvironment factors that involved in many biological processes. Cell dysfunctions such as cell apoptosis, lysosomal membrane permeabilization (LMP), mitochondrial membrane depolarization were also closely associated with pH_i fluctuation. Cellular acidification has been proposed as the main origin for silicosis induced by crystalline silica [1,2]. Therefore, sensing *in situ* pH_i oscillation is of great significance for clarifying these physiological and pathological processes. With the excellent spatiotemporal resolution, fluorescent imaging especially the ratiometric imaging has become one of the most important tools to provide the accurate in-

*Corresponding authors (email: heweij69@nju.edu.cn; zguo@nju.edu.cn)

formation of pH_i. A few of ratiometric pH_i sensors have been reported so far showing the different design strategies or sensing mechanism, such as nanoparticle/fluorophore hybridization [3,4], dual fluorescent protein integration [5], and dual fluorophore dyad [6]. However, cells are highly compartmentalized to provide diversified microenvironments of different physicochemical properties, such as pH_i [7], and temperature [8,9], to realize their respective physiological functions. The different pH_i in diversified intracellular microstructures demands ratiometric fluorescent pH_i sensors with different subcellular compartment targetability, sensing range, and sensitivity. Therefore novel approach to ratiometric pH_i sensors is always appealing to construct ratiometric pH_i sensor to meet the diversified requirement. Since aggregation-induced emission (AIE) shows no sensor concentration-related ACQ (aggregation caused quenching) interference in fluorescence sensing [10–13], the typical AIE fluorophore tetraphenylethene (TPE) has been conjugated with a cyanine fluorophore to form TPE-Cy dyad for ratiometric pH_i sensing [14–16]. Modifying classic fluorophore to show both AIE and intrinsic emission for dual emission ratiometric sensing might be another promising approach to ratiometric pH_i sensors.

In this study, BODIPY fluorophore was modified with a pH sensitive group benzimidazole on its β-position to form three 2-(benzoimidazol-2-)yl-1,3,5,7-tetramethyl-BODIPY derivatives, **BBI-1/2/3** (Scheme 1). The pH-induced transition between their BODIPY intrinsic emission and AIE were observed for all the three compounds favouring ratiometric pH sensing. The regulation of pH sensing range was achieved by modifying benzimidazole with different substituents. Moreover, the silica exposure-induced cellular acidification of A549 cells was monitored successfully via **BBI-1** staining, and the synchronization of the silica-induced lysosome disruption to cellular acidification was observed directly for the first time.

2 Experimental

2.1 Materials and general methods

All reagents for synthesis were commercially available and utilized directly without further purification. LysoTracker Deep Red was from Thermo Fisher Scientific (USA). The spectroscopically pure solvents were from Tedia and the deionized water from a Millipore system (>18.2 MΩ, USA) were utilized for spectroscopic study. The stock solutions of all the tested compounds were prepared by dissolving NaCl, KCl, $MgCl_2$, $CaCl_2$, $ZnCl_2$, $CuCl_2$, $FeCl_3$, $FeCl_2$, NH_4Cl, Ca$(ClO)_2$, NaHS, *L*-cysteine (Cys), glutathione (GSH), homocysteine (Hcy), and H_2O_2 (30% solution) in the deionized water. The reactive oxygen species (ROS) were prepared according to the reported procedures [17,18]. The ^{1}H NMR and ^{13}C NMR spectra were recorded on Bruker Avance DRX-400 (Germany) with TMS as the internal reference. High resolution mass spectrometric data were determined using an Agilent 6540Q-TOF HPLC-MS spectrometer (USA). Fluorescence spectra were determined using a Horiba FluoroMax-4 spectrofluorometer (Japan). Absorption spectra were recorded using a Perkin Elmer Lambda35 spectrophotometer (USA). Dynamic light scattering (DLS) tests and transmission electron microscope (TEM) images were accomplished using Brookhaven BI-200SM particle size analyzer (USA) and JEOL JEM-2100 (Japan), respectively. The surface area of small particles (silica and titanium oxide) was determined by Micromeritics ASAP2020 M+C. Solution pH was adjusted to the desired values by 1 M HNO_3 or 1 M NaOH and measured with a Model PHS-3C meter just before the determination of UV-vis and fluorescence spectra. Fluorescence quantum yield of **BBIs** were determined using an integrating sphere, and absorbance of samples at their respective excitation wavelengths were controlled to be lower than 0.05.

2.2 Synthesis of BBI-1/2/3

Synthesis of compound **2**. Compound **2** (Scheme 2) was synthesized from compound **1**, which was prepared by a reported procedure [19,20]. Therefore, anhydrous *N*,*N*-dimethylformamide (DMF) and $POCl_3$ were mixed with stirring under N_2 atmosphere in a bottom flask in a cooling bath. After being stirred at room temperature for 30 min, the mixture was added with compound **1** (1 mmol, 382 mg) dissolved in CH_2Cl_2. Then the mixture was stirred at 50 °C and monitored with thin layer chromatography (TLC) till compound **1** disappeared. Then the mixture was poured into 150 mL saturated $NaHCO_3$ solution at 0 °C and stirred for another 30 min. After separation, the aqueous phase was extracted twice with CH_2Cl_2. The combined organic phases were washed three times with water and dried over anhydrous Na_2SO_4. After evaporation *in vacuo* to remove solvent, the residue was purified by silica gel chromatography (petroleum ether: CH_2Cl_2=50:1, *v*/*v*) to afford the product (387 mg) as orange solid. Yield, 94%. ^{1}H NMR (400 MHz, $CDCl_3$) δ 10.03 (s, 1H), 8.25 (d, 2H), 7.45 (d, 2H), 6.19 (s, 1H), 4.01 (s, 3H), 2.85 (s, 3H), 2.65 (s, 3H), 1.67 (s, 3H), 1.43 (s, 3H) ppm. ^{13}C NMR (100 MHz, $CDCl_3$) δ 166.20, 162.24, 156.95, 146.91, 142.19, 142.11, 138.90, 133.66,

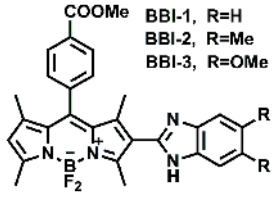

Scheme 1 Chemical structures of **BBI 1/2/3**.

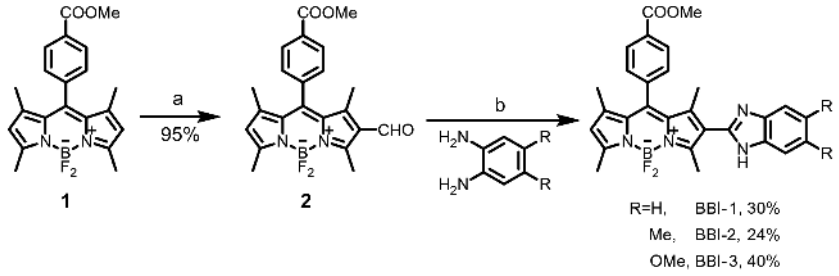

Scheme 2 Synthesis of compounds **BBIs**. Reagents and conditions: (a) DMF, $POCl_3$, $ClCH_2CH_2Cl$, 50 °C, 2 h; (b) *p*-TSA, DMF, reflux, overnight.

131.42, 130.66, 129.31, 128.19, 126.49, 124.32, 52.47, 15.13, 14.97, 13.01, 11.75 ppm. HR-MS (ESI, positive mode, *m*/*z*): found 411.1697, calcd. 411.1692 for $[M+H]^+$.

General procedure for the synthesis of **BBI-1/2/3**. Compound **2** (0.5 mmol, 205 mg), *o*-phenylenediamine (0.8 mmol) and *p*-toluenesulfonic acid monohydrate (0.1 mmol, 19.0 mg) were mixed in 8 mL DMF and refluxed at 150 °C overnight and monitored with TLC. After the consumption of compound **2**, the reaction mixture was poured into ice water followed by filtration. The solid was washed by water and dried in vacuo. The final product was obtained via purifying the crude product with silica gel chromatography.

BBI-1: Petroleum ether/EtOAc (3:1, *v*/*v*). The product was obtained as dark orange solid (76 mg). Yield, 30%. ^{1}H NMR (400 MHz, DMSO-d_6) δ: 8.18 (d, 2H), 7.67 (d, 2H), 7.57 (bs, 2H), 7.19 (s, 2H), 6.35 (s, 1H), 3.92 (s, 3H), 2.67 (s, 3H), 2.54 (s, 3H), 1.50 (s, 3H), 1.37 (s, 3H) ppm. ^{13}C NMR (100 MHz, DMSO-d_6) δ: 166.19, 158.87, 153.71, 146.42, 145.18, 141.89, 139.86, 139.18, 131.96, 131.75, 131.01, 130.63, 129.74, 129.15, 125.38, 123.50, 123.01, 122.32, 52.93, 14.97, 14.87, 13.93, 13.13 ppm. HR-MS (ESI, positive mode, *m*/*z*): found 499.2119, calcd. 499.2117 for $[M+H]^+$.

BBI-2: Petroleum ether/EtOAc (3:1, *v*/*v*). The product was obtained as dark orange solid (68 mg). Yield, 24 %. ^{1}H NMR (400 MHz, DMSO-d_6) δ 8.18 (d, J=8.2 Hz, 1H), 7.64 (d, J= 8.2 Hz, 1H), 7.33 (s, 1H), 6.33 (s, 1H), 3.91 (s, 3H), 2.63 (s, 3H), 2.30 (s, 3H), 1.47 (s, 3H), 1.37 (s, 3H) ppm. ^{13}C NMR (100 MHz, DMSO-d_6) δ 165.95, 158.39, 153.47, 144.99, 144.76, 141.49, 139.49, 138.86, 131.55, 130.67, 130.35, 129.44, 128.81, 123.11, 123.00, 52.62, 20.09, 14.62, 14.46, 13.58, 12.78 ppm. HR-MS (ESI, positive mode, *m*/*z*): found 527.2429, calcd. 527.2430 for $[M+H]^+$.

BBI-3: Compound 1,2-diamino-4,5-methoxybenzene, was synthesized with the reported procedure [21,22]. The chromatography eluent was CH_2Cl_2/EtOAc (25:1, *v*/*v*), and the product was obtained as dark purple solid (103 mg). Yield, 40%. ^{1}H NMR (400 MHz, DMSO-d_6) δ: 8.17 (d, 2H), 7.65 (d, 2H), 7.09(bs, 2H), 6.32 (s, 1H), 3.91 (s, 3H), 3.78 (s, 6H), 2.64 (s, 3H), 2.53 (s, 3H), 1.48 (s, 3H), 1.36 (s, 3H) ppm. ^{13}C NMR (100 MHz, DMSO-d_6) δ: 166.19, 158.31, 154.00, 146.90, 144.79, 144.78, 141.72, 139.25, 131.76, 130.98, 130.63, 129.78, 129.16, 128.50, 126.86, 123.56, 123.27, 56.34, 52.93, 14.93, 14.77, 13.98, 13.10 ppm. HR-MS (ESI, positive mode, *m*/*z*): found 559.2330, calcd. 559.2338 for $[M+H]^+$.

2.3 Cell culture and confocal imaging

Adenocarcinomic human alveolar basal epithelial cells (A549 cells) were cultured in RPMI1640 medium containing 10% fetal bovine serum (FBS; Gibco) at 37 °C in a humidified atmosphere with 5% CO_2. For confocal fluorescent imaging, A549 cells were seeded at 40% confluence in a glass bottom dish (φ 2 mm; NEST) with 1 mL culture media.

The imaging was carried out with a confocal laser scanning fluorescence microscope (Zeiss LSM710, Germany) with a 63× oil objective lens. For pH_i calibration, A549 cells were stained by **BBI-1** (10 μM) in phosphate buffer saline (PBS) (20 mM, pH 7.4, 1% DMSO) for 10 min and rinsed with PBS (1×) for 3 times. Then the cells were treated with 1 mL high K^+ buffers (125 mM KCl, 20 mM NaCl, 20 mM PBS) of different pH (3.8–6.5) in the presence of 5.0 μM nigericin. After imaging respectively with a dual excitation/dual emission mode (green channel for the intrinsic emission of **BBI-1**, I_{int}: λ_{ex} 488 nm, bandpath: 495–540 nm; red channel for AIE of **BBI-1**, I_{agg}: λ_{ex} 543 nm, bandpath 550–700 nm), the ratiometric (I_{int}/I_{agg}) images and the related I_{int}/I_{agg} ratio values were obtained using Zen 2008 software equipped on the microscope.

To clarify the intracellular distribution pattern of **BBI-1**, its co-localization experiments with MitoTracker Deep Red FM, LysoTracker Deep Red and Hoechst 33342 were carried out, respectively. For each experiment, A549 cells were firstly stained with the organelle dye with the standard procedure offered by the commercial supplier followed by staining with **BBI-1** (10 μM). The imaging bandpath for MitoTracker Deep Red FM is 650–720 nm (λ_{ex}, 633 nm), for LysoTracker Deep Red, 640–700 nm (λ_{ex}, 633 nm), for Hoechst 33342, 410–480 nm (λ_{ex}, 405 nm), for **BBI-1**, 495–630 nm (λ_{ex}, 488 nm).

For imaging of A549 cells upon small particle exposure, the crystalline silica Min-U-Sil 5, Min-U-Sil 10, amorphous

nanosilica, and nano-titanium dioxide were commercial available. The particles were washed three times with distilled water and then dried overnight at 95 °C to remove endotoxin [23]. Then the particles were suspended in distilled water (1 mg/mL) followed by sonication for 30 min, and the obtained suspensions were stored in fridge at 4 °C. The suspensions were sonicated for 30 min before each use. The sonicated suspension was then added into RPMI1640 medium without serum (Gibco) or PBS to the desired concentration (50 μg/mL). The **BBI-1** stained cells were then cultured with the obtained media for 12 h or the desired time. After being rinsed 3 times with PBS, the cells were imaged in the same dual excitation/dual emission mode.

For confocal imaging of A549 cells co-stained by LysoTracker Deep Red and **BBI-1**, the cells were stained with 75 nM LysoTracker Deep Red for 2 h and then **BBI-1** (10 μM, 20 mM PBS, pH 7.4, 1% DMSO) for 10 min at 37 °C. After being washed with PBS buffer for 3 times, the cells were treated with 50 μg/mL MUS 5 suspended in PBS and then imaged. The LysoTracker channel images were obtained with a bandpath from 640–700 nm upon excitation of 633 nm, and the ratiomeric imaging for pH_i was realized with same dual exciation/dual emission mode showed above. The cells incubated with PBS were also imaged as a control.

2.4 Cytotoxicity assay

The cytotoxic behaviors of all the **BBI** molecules were evaluated using the MTT assay against A549 cells. Cells (2000 cells/well) were seeded on a 96-well plate in 100 μL of RPMI1640 (Gibco) medium and incubated for 24 h. The cells were treated with **BBI** probes at varying concentrations (from 1 to 20 μM in PBS buffer solutions) and incubated for 12 h at 37 °C. The cells were then treated with 20 μL of MTT (5 mg/mL in PBS) for 5 h. The medium was removed, the cells were lysed with 100 μL of DMSO, and the absorbance of the purple formazan was recorded at 550 nm using a Bio-Tek Synergy HT microplate reader. All tests were carried out in triplicate.

3 Results and discussion

3.1 Idea for BBIs' pH sensing and BBIs preparation

BODIPYs featuring excellent spectroscopic properties such as high photochemical stabilities and quantum yield, were frequently utilized to construct fluorescent sensors and labelling agents [24]. Besides photoinduced electron transfer (PeT) and intramolecular charge transfer (ICT) [25], the newly reported AIE of BODIPYs provided the additional approach to BODIPY-based sensor [26–28], and the different response of AIE and intrinsic emission of BODIPYs to specific target, such as proton, could be a promising alternative for ratiometric sensing. In this study, BOIDPY was coupled with a reversible pH sensing group 2-benzimidazole [29] via a rotatable C_{sp2}–C_{sp2} bond, which is the normal characteristic structure for AIE fluorophore, to explore the possibility of different pH response of BODIPY emission and AIE.

BBI-1 was prepared easily via condensation of 2-formyl-BODIPY with *o*-phenylenediamine (Scheme 2). The substituents on benzimidazole moiety, were introduced to alter the proton binding ability of benzimidazole N atom, and **BBI-2/3** were synthesized in the similar procedure. All the compounds were fully characterized by ^1H and ^{13}C NMR, and high resolution mass spectrometry (Figures S1–S9, Supporting Information online).

3.2 Fluorescent pH response of BBI-1/2/3

Different from the "on-off" pH sensors with BODIPY/benzimidazole skeleton showing only the single intrinsic emission band of BODIPY at ~510 nm [30,31], **BBI-1** displayed two emission bands in neutral PBS buffer (pH 7.2) upon excitation at 488 nm: one sharp band centered at 510 nm and one broad band (540–750 nm) with a maximum at ~595 nm (Figure 1(a)). The former was assigned as the intrinsic emission band of BODIPY, and the latter the AIE band. The assignment of AIE band was supported by the nanoparticles found in **BBI-1** solution (*vide infra*). Decreasing pH of **BBI-1** solution from 7.2 to 6.5 led to the AIE descent and the intrinsic emission enhancement (Figure 1(a)). The drastically enhanced intrinsic emission band at even lower pH overlaid the decreased AIE band, and the ratiometric pH sensing behaviour of **BBI-1** was concealed. The ratiometric pH sensing behaviour was retained when BODIPY intrinsic emission and AIE were excited respectively at 488 and 543 nm, and the rise of intrinsic emission (I_{int}, Figure 1(b)) and the fall of AIE (I_{agg}, Figure 1(c)) were observed simultaneously upon pH falling from 7.4 to 3.0. Therefore the I_{int}/I_{agg} ratio was distinctly enhanced showing the pH ratiometric sensing capability via a dual excitation/dual emission mode. The pK_a of **BBI-1** were determined as 4.4 by fitting the ratio I_{int}/I_{agg} with nonlinear sigmoid equation (Figure 1(d)). In the meantime, the fluorescence of **BBI-1** solution under UV lamp turned from dim red to bright green upon acidification from pH 6.0 to 1.0 (Figure S10).

Similarly, **BBI-2** and **BBI-3** showed the dual emission band in neutral PBS. Both compounds displayed the ratiometric pH sensing behaviour via determining the intrinsic emission and AIE respectively upon the respective excitation at 488 and 543 nm (dual excitation/dual emission, Figure S11). The pK_a values for **BBI-2** and **BBI-3** were determined as 2.7 and 3.6 via fitting the pH-dependent profile of I_{int}/I_{agg}. The 5,6-dimethyl groups of **BBI-2** and 5,6-dimethoxyl groups of **BBI-3** should be responsible for their different pK_a.

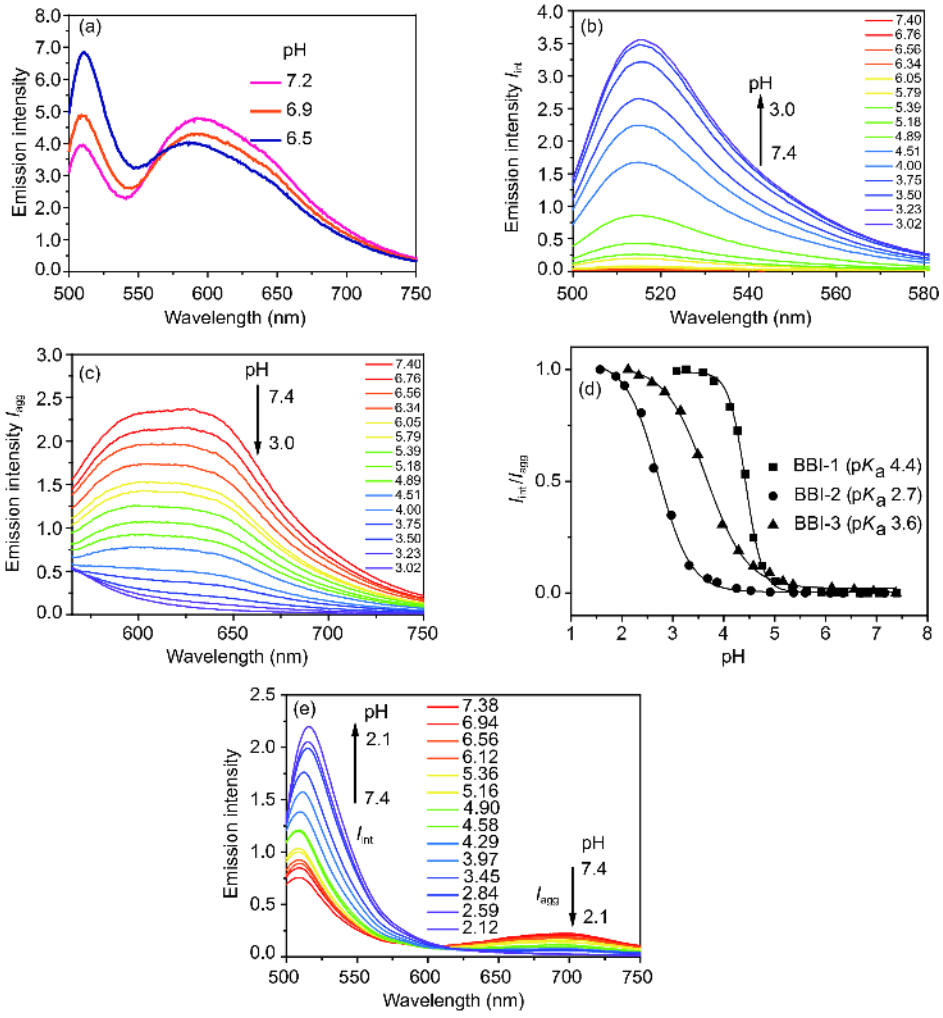

Figure 1 (a) Fluorescence spectra of 10 μM **BBI-1** in PBS buffers (20 mM, 1% DMSO) of pH 7.2, 6.9, and 6.5. λ_{ex}: 488 nm. (b) Intrinsic emission (I_{int}, λ_{ex}: 488 nm) and (c) AIE (I_{agg}, λ_{ex}: 543 nm) spectra of 10 μM **BBI-1** in PBS buffers (20 mM, 1% DMSO) determined at pH 3.0–7.4. (d) Fluorescence intensity ratio I_{int}/I_{agg} of **BBI-1**, **BBI-2** and **BBI-3** determined at different pH, the fitting lines and the calculated pK_a. (e) Fluorescence spectra of 10 μM **BBI-3** in PBS buffer (20 mM, 1% DMSO) determined at pH 7.4–2.1 upon excitation at 488 nm (color online).

This gave the hints to regulate the pH sensing range by modifying benzimidazole with different substituents. For **BBI-3**, the emission spectra determination showed the distinct ratiometric pH sensing ability from pH 7.4 to 2.1 even upon single excitation at 488 nm. This provided **BBI-3** still the dual emission mode for ratiometric pH sensing (Figure 1 (e)).

3.3 pH-regulated aggregation of BBIs in neutral aqueous medium

BBI-1 showed the typical sharp absorption band (centred at 496 nm) of BODIPY at pH 3.0 (Figure 2(a)). This implied that β-benzoimdazol-2-yl group might not conjugate with BODIPY. Increasing pH from 3.0 to 4.8 led to the drop of this sharp band and the emergence of broad band centered at 550 nm. This new band increased with pH increases, and an isobestic point at 512 nm was observed. The drastic enhancement of this new band above pH 4.8 made this band overlap the decreased BODIPY absorption at 496 nm to form a broad band centred at 527 nm (Figure 2(b)). The pH-induced colorimetric change from pink to yellow was also observed (Figure S10). UV-visible pH titration of **BBI-2** and **BBI-3** showed the similar pH-dependent absorption change (Table S1, Figure S12, Supporting Information online).

Although the neutral aqueous solutions (1% DMSO) of **BBI-1** was homogeneous and transparent even with water content as high as 99%, the dynamic light scattering (DLS) determination of **BBI-1** solution (10 μM) demonstrated that there were nanoparticles of ~90 nm in the solution. The transmission electron micrograph (TEM) imaging confirmed the uniform nanoparticles formed in the solution of **BBI-1** (Figure 3(a, b)). However, DLS and TEM determination found there were no nanoparticles formed in **BBI-1** aqueous solution of pH 3.0, and the absorption spectra showed only the typical sharp BODIPY absorption band. All these sug-

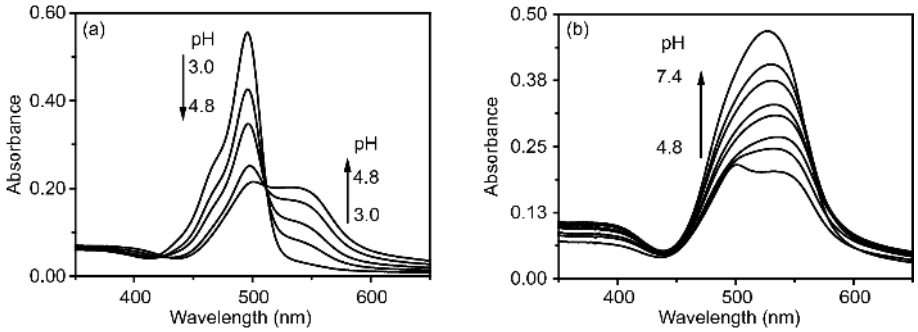

Figure 2 Absorption spectra of **BBI-1** (20 μM) in PBS buffers (20 mM, 2% DMSO) determined at pH (a) 3.0–4.8 and (b) pH 4.8–7.4.

gested that **BBI-1** in neutral aqueous medium tended to aggregate, and the broad emission band spanning from 540 to 750 nm in Figure 1(a) could be assigned as an AIE band. The absorption bathochromic shift found upon pH increasing from 3.0 to 4.8 was proposed to be induced by intermolecular aggregation. The benzimidazolium deprotonation-induced **BBI-1** aggregation might be correlated to the lower aqueous solubility of **BBI-1** than its protonated form. The aqueous solution of **BBI-2** and **BBI-3** demonstrated also the nanoparticles in neutral aqueous solution and the AIE bands (Figure S13). The AIE behavior of **BBI-1** was further confirmed by its emission spectra in ethanol/water mixed solvents of different water fraction f_w (Figure S14). **BBI-1** shows very weak emission at 630 nm at f_w<75%. The higher water fraction (f_w >75%) leads to the distinct emission enhancement, and the maximum of this band was observed at f_w =92.5%. The similar AIE behavior has also been found for both **BBI-2** and **BBI-3**. The minor decrease from the maximum AIE at even higher water content might be caused by the alteration of sensor conformation and packing mode in the aggregates [32,33].

The aggregation of the three compounds in neutral aqueous solution was consistent with their structures. Structure resolution of **BBI-2** crystals (Table S2) revealed that the dihedral angle between BODIPY plane and benzimidazole was 19.5°, while that between BODIPY and *meso*-phenyl group was almost 77.4°. Moreover, there was no π-π interaction in the crystal, and the hydrogen bond N–H···F with distance of 2.55 Å was found between benzimidazole NH and F atom from another BODIPY molecule (Figure 3(c)). The non-coplanarity disclosed by the two dihedral angles and this intermolecular hydrogen bond resulted in the absence of intermolecular π-π interaction, which inferred that the broad emission band spanning from 540 to 750 nm was not an excimer emission band. On the contrary, the absence of π-π interaction excluded the ACQ effect of emission and favoured the AIE in solids or aggregates. In fact, powders of both **BBI-1** and **BBI-2** demonstrated the distinct solid fluorescence at ~645 nm, and the broad emission band spanning from 540 to 750 nm in emission spectrum of **BBI-1**

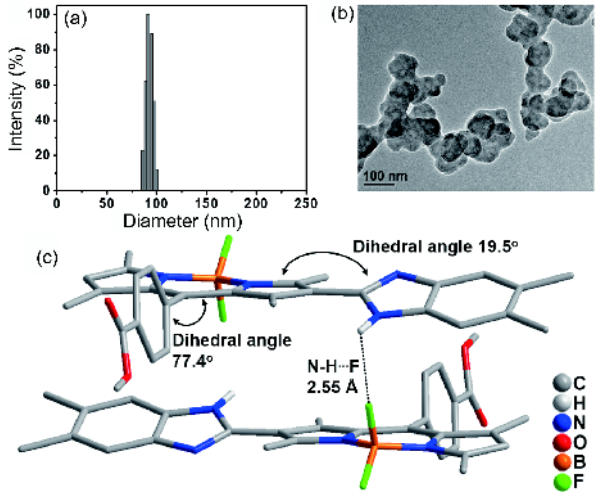

Figure 3 (a) Hydrodynamic diameter of aggregates in **BBI-1** (10 μM) solution in water (1% DMSO) determined by dynamic light scattering test. (b) Transmission electron microscopic image of the same **BBI-1** solution. Scale bar: 100 nm. (c) N–H···F hydrogen bond and dihedral angles in **BBI-2** disclosed by crystal resolution. Most hydrogen atoms were omitted for clarity (color online).

and **BBI-2** in neutral aqueous solution can be assigned as AIE band. The red shift of AIE from the intrinsic emission was ascribed to the hydrogen bond-related energy transfer in excited state [34].

The non-coplanarity of benzimidazole and BODIPY indicated that benzimidazole moiety was not involved in the conjugated system of BODIPY, therefore PeT from imidazole to BODIPY was proposed to quench the emission of **BBI**, and the protonation of imidazole not only blocked this PeT effect but also triggered the transition from AIE to intrinsic emission, which enhance the intrinsic emission simultaneously.

3.4 Ratiometric pH sensing behavior of BBIs

The pH-specific sensing behavior of **BBI-1** was investigated via determing the ratio of intrinsic emission to AIE, I_{int}/I_{agg}, in the presence of different physiological species such as metal cations, ROS and biothiols. The decrease of pH from 7.4 to

3.0 led to the distinct enhancement of I_{int}/I_{agg}. However, no obvious alteration of I_{int}/I_{agg} was observed upon adding these chemical species (Figures 4(a)). This result confirmed the specific pH sensing ability of **BBI-1**. Moreover, this ratiometric pH sensing behavior was reversible at least in the initial five cycles of pH oscillation between 7.4 and 3.0 (Figure 4(b)), indicating both the protonation and the aggregation were reversible. **BBI-2** and **BBI-3** displayed the similar pH fluorescent sensing behaviours including the sensing selectivity and reversibility (Figures S15, S16).

3.5 pH_i imaging in human epithelial lung cancer cells (A549) with BBI-1

The sensor cytotoxicity against A549 cells has been determined with MTT assay. After incubating the cells with 10 μM sensor at 37 °C for 12 h, the cell viability is above 82% in the case of **BBI-1** (Figure S17), showing the fine bocompatiability of this sensor. Although the biocompatibility of **BBI-2** and **BBI-3** is poorer than **BBI-1**, the cell viability is still higher than 70% at the same condition. Among the three **BBI** sensors, **BBI-1** displayed a pK_a of 4.4, and the linear pH-sensitive range from pH 3.5 to 5.5. This made it suitable for pH determination in acidic subcellular compartments especially in the process of cellular acidification. The pH_i imaging ability of **BBI-1** was investigated with human epithelial lung cancer cells (A549 cells) stained by **BBI-1** (10 μM, 10 min at 25 °C).

A549 cells can be stained within 10 min by 10 μM **BBI-1** (20 mM PBS, pH 7.4, containing 1% DMSO) showing the fine membrane permeability of this sensor. To clarify the intracellular distribution pattern of **BBI-1**, A549 cells were co-stained with **BBI-1** and commercially available dyes such as MitoTracker Deep Red FM, LysoTracker Deep Red and Hoechst 33342. The results disclose that **BBI-1** fluorescence distributes in cytoplasm with no specific target (Figure S18), and the nonspecific distribution would contribute to the tracking of cytoplasm acidification.

To determine the pH_i calibration curves of **BBI-1** in A549 cells, the **BBI-1** stained cells were incubated with buffers of different pH containing nigericin, which was utilized to uniform intracellular and extracellular pH [35]. Then the cells were imaged with a dual excitation/dual emission model (green channel for I_{int}: λ_{ex} 488 nm, bandpath 500–540 nm; red channel for I_{agg}: λ_{ex} 543 nm, bandpath 550–700 nm) to offer the green and red channel images respectively. The green channel images disclosed that I_{int} was enhanced with pH decreasing from 6.5 to 3.8, whereas I_{agg} in red channel images decreased gradually in the mean time (Figures 5(a) and S19). The ratiomeric images of green to red channel images (I_{int}/I_{agg}) exhibited that the mean I_{int}/I_{agg} ratio in the cells increased linearly with the pH drecease from pH 6.0 to 3.8 (Figure 5(b)). Linear fitting of I_{int}/I_{agg} profile gave a calibration formula (**I**): I_{int}/I_{agg}=83.2–13.6pH (R^2=0.992, R, the correlation coefficient).

3.6 Ratiometric pHi monitoring in A549 cells upon silica exposure

Long-term inhalation of crystalline silica usually occurs in silica milling, rock drilling and tunneling, which leads to silicosis. Crystalline silica exposure was also associated with other diseases and disorders such as tuberculosis, airway obstruction, lung cancer, and autoimmune diseases [36–49]. In addition, oxidative stress [40,41], inflammasome activation [42], cytokine release and excessive apoptotic cell death have been proposed to be involved in the pathologies of these disorders, which were complicated and demanded further elucidation. Since the internalized particles were normally entrapped in lysosomal compartments [43], lysosomal dysfunction was recognized as the main toxic effect of small particles [1], and the resulted massive LMP led to the acidic matrix translocation from lysosomal lumen to the cytosol. This cellular acidification was proposed to trigger the mi-

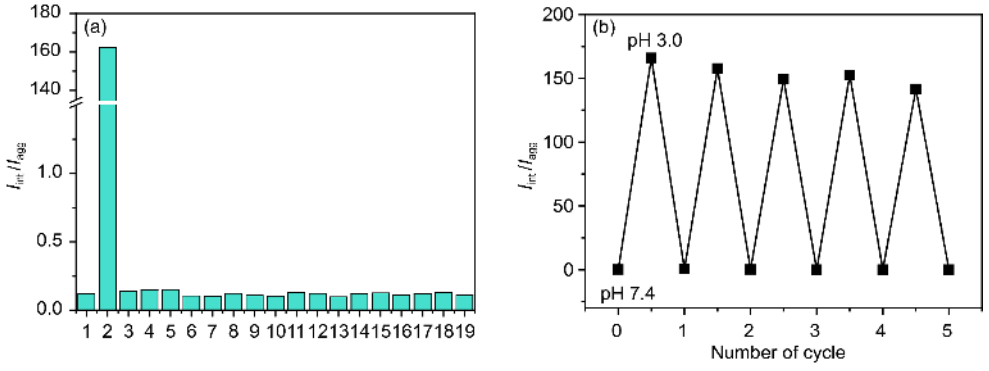

Figure 4 (a) Fluorescence intensity ratio I_{int}/I_{agg} of **BBI-1** (10 μM) in PBS buffer (20 mM, 1% DMSO) determined at pH 7.4 (1, blank), pH 3.0 (2), or after the addition of (3–19): 3, K^+; 4, Na^+; 5, Ca^{2+}; 6, Mg^{2+}; 7, NH_4^+ (3–7: 1 mM); 8, Zn^{2+}; 9, Fe^{2+}; 10, Fe^{3+}; 11, Cu^{2+} (8–11: 10 μM); 12, H_2O_2; 13, O_2^-; 14, ClO^-; 15, $^1O_2$; 16, glutathione; 17, cysteine (12–17: 1 mM); 18, HS^-; 19, homocysteine (18, 19: 100 μM). (b) Fluorescence intensity ratio I_{int}/I_{agg} of **BBI-1** (10 μM) in PBS buffer (20 mM, 1% DMSO) determined in the initial five cycles of pH oscillation between 7.4 and 3.0 (color online).

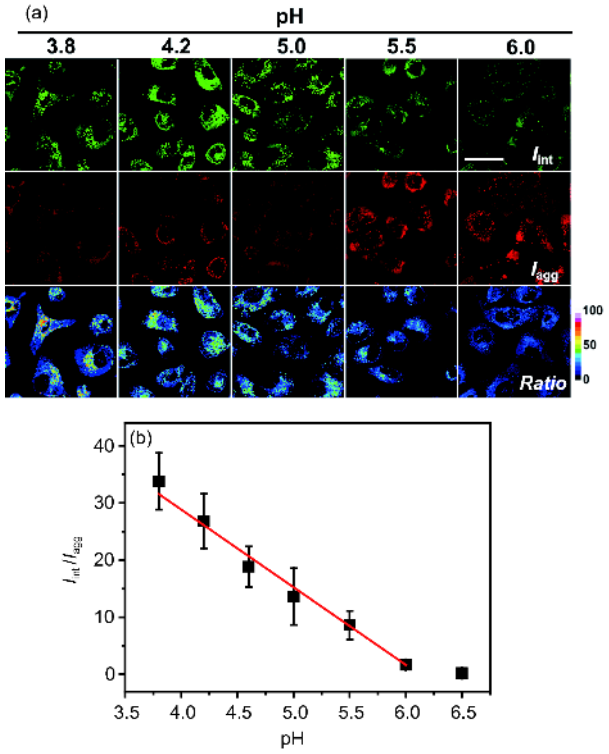

Figure 5 (a) Ratiometric imaging (I_{int}/I_{agg}) of A549 cells stained by 10 μM **BBI-1** (10 min at 25 °C). The stained cells were incubated with high K^+ buffers (125 mM KCl, 20 mM NaCl, 20 mM PBS) of different pH (3.8–6.0) in the presence of 5.0 μM nigericin followed by imaging respectively with a dual excitation/dual emission mode (green channel for I_{int}: λ_{ex} 488 nm, bandpath 500–540 nm; red channel for I_{agg}: λ_{ex}543 nm, bandwidth 550-700 nm). Scale bar: 20 μm. The ratiometric (I_{int}/I_{agg}) images were given automatically based on the green and red image pairs by microscope LSM710. (b) Mean I_{int}/I_{agg} ratios in the ratiometric images at different pH and the linear fitting line of I_{int}/I_{agg} ratio from pH 3.8 to 6.0. Data were calculated as average values for each cell and presented as mean ±standard deviation (N=7, based on three independent experiments) (color online).

tochondria depolarization and caspase activation [44,45]. Therefore, monitoring pH_i *in situ* via fluorescence imaging is of great significance to clarify the LMP-related diseases induced by crystalline silica exposure.

With the pH_i calibration formula I and the pH_i imaging ability in pH 3.8–6.5, **BBI-1** was adopted to track pH_i fluctuation in A549 cells with crystalline silica exposure, which was utilized as the cell model for silicosis. Commercially available microscale crystalline silica Min-U-Sil 5 (MUS 5) and Min-U-Sil 10 (MUS 10) were suspended in cell culture media to investigate the pH_i fluctuation, while amorphous nanosilica (ANS) and nanotitanium dioxide (NTO) were also investigated for comparison. The surface areas and particle sizes of these particles were summarized in Table S3 (Figures S20–S22). The **BBI-1**-stained A549 cells were cultured in media containing 50 μg/mL MUS 5, MUS 10, ANS or NTO for 12 h, followed by confocal imaging with the dual excitation/dual emission mode. With the intracellular I_{int}/I_{agg} ratios determined in the ratiometric images, the average pH_i for the **BBI-1**-distributed area in A549 cells cultured in RPMI1640 medium without serum was determined as 5.85 ±0.10. MUS 5 incubation made the detected pH_i decrease to 4.44±0.14, while MUS 10 to 5.21±0.10 (Figures 6 and S23), although both MUS 5 and MUS 10 were crystalline silica. The different pH_i induced by MUS 10 and MUS 5 could be ascribed to their different particle size (MUS 5, 3.5±1.5 μm, MUS 10, 4.0±2.0 μm) and surface area (MUS 5, ~6.76 m^2/g, MUS 10, ~1.07 m^2/g). The more distinct pH_i drop induced by MUS 5 indicated that the smaller micronscale crystalline silica with larger surface area is more effective to induce cellular acidification.

Although ANS with smaller size was reported to show higher cell toxicity [46,47], ANS with the size of 10.0±4.0 nm was found to reduce pH_i to 4.95±0.20, which was higher than that inuced by MUS 5 and lower than that induced by MUS 10. However, pH_i upon nano-TiO_2 (8±3 nm) exposure was determined as 5.84±0.05, which was almost identical to that of control. This was consistent with the reported inertness of nano-TiO_2 even when internalized into biological system [48,49].

The direct observation of crystalline silica-induced lysosomal disruption assoicating with acidification was also achieved for the first time by imaging the crystalline silica-incubated A549 cells via constaining with **BBI-1** and LysoTracker Deep Red. The three-channel mode (ratiomertic pH_i imaging: green channel for I_{int}: λ_{ex} 488 nm, bandpath 500–540 nm, red channel for I_{agg}: λ_{ex} 543 nm, bandwidth 550–630 nm; LysoTracker channel: λ_{ex} 633 nm, bandpath: 640–700 nm) was adopted for the imaging. The ratiometric pH_i images (I_{int}/I_{agg}) for the cells incubated with PBS buffer

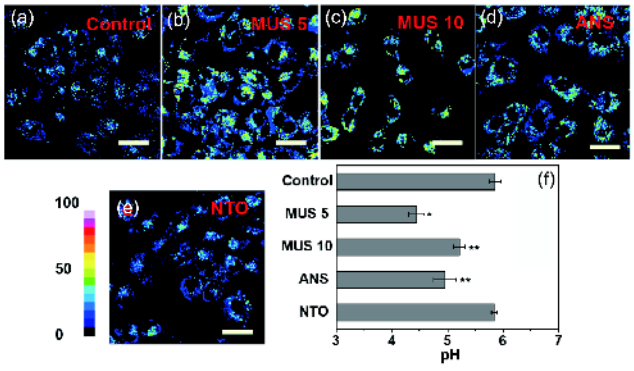

Figure 6 (a–e) Fluorescence ratiometric (I_{int}/I_{agg}) images of A549 cells stained by 10 μM **BBI-1** (10 min at 25 °C) followed by incubation with (a) RPMI1640 medium without serum, or RPMI1640 medium without serum suspended with 50 μg/mL (b) MUS 5, (c) MUS 10, (d) ANS, and (e) NTO for 12 h. Scale bar: 20 μm. The ratiometric images were mediated from the related green (I_{int}: λ_{ex}488 nm, bandpath 500–540 nm) and red (I_{agg}: λ_{ex} 543 nm, bandpath 550–700 nm) channel images automatically by confocal microscope LSM710. (f) The calculated average pH_i in A549 cells in (a–e). Data were calculated as average values for each cell and were presented as mean ± standard deviation (N=7, three independent experiments) (color online).

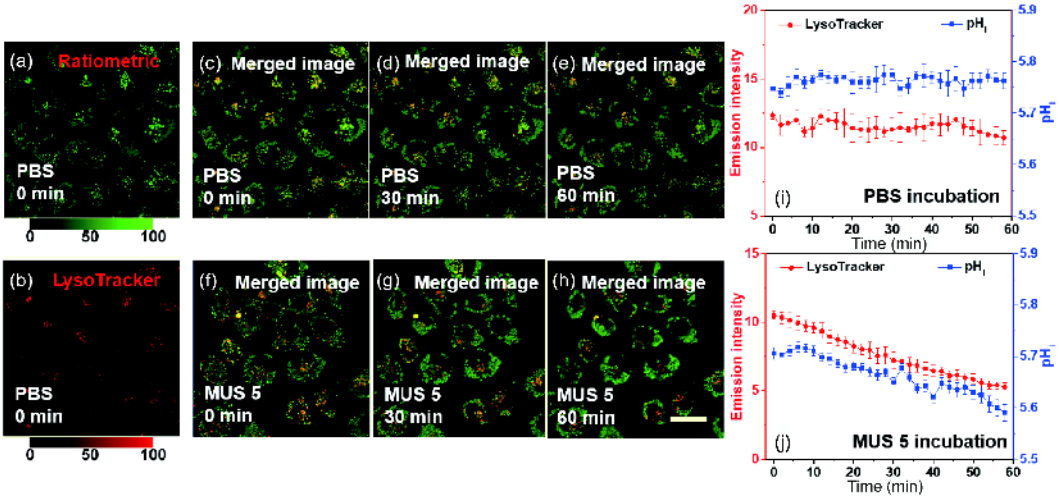

Figure 7 Confocal imaging of A549 cells stained by LysoTracker Deep Red (75 nM,2 h at 25 °C) and **BBI-1** (10 μM,10 min at 25 °C) upon incubation (1 h) with PBS (20 mM, pH 7.4; a–e) and PBS suspended with crystalline silica MUS 5 (50 μg/mL, f–h). (a) Ratiometric image (I_{int}/I_{agg}) obtained from the green (I_{int}: λ_{ex}488 nm, bandpath 500–540 nm) and red (I_{agg}: λ_{ex}543 nm, bandpath 550–630 nm) channel image pair recorded at the beginning of PBS incubation; (b) LysoTracker channel image (λ_{ex}633 nm, bandpath 640–700 nm) of cells in (a); (c) merged image of ratiometric image (a) and LysoTracker channel image (b); and the merged images of cells obtained after 30 min (d) and 60 min (e) of PBS incubation. (f–g) Merged images of ratiometric pH$_i$ image (I_{int}/I_{agg}) and LysoTracker image of A549 cells obtained at (f) 0, (g) 30 and (h) 60 min upon incubation with PBS buffer suspended with MUS 5. Scale bar: 20 μm. (i, j) The related temporal profiles of pH$_i$ (green) and intracellular LysoTracker fluorescence intensity (red). Data were calculated as average values for each cell and were presented as mean ± standard deviation (N=7 cells) (color online).

disclosed that pH$_i$ was ~5.75 (Figure 7(a)). Imposing this pseudocolor ratiometric pH$_i$ image on the related LysoTracker image (Figure 7(b)) dislcosed that almost all the red signal for LysoTracker was covered by the green signal in ratiometric image to show the yellow signal as lysosome. There was still many green signals distributed randomly inside the cell besides the yellow spots, indicating the intracellular distribution of **BBI-1** was not limited in lysosome (Figure 7(c)).

Temporal ratiometric pH$_i$ tracking in 1 h disclosed that there was no distinct pH$_i$ change regardless of the slight photo-bleaching in red and green channel images (Figure 7 (i)). In the mean time, LysoTracker channel images showed also the stable red fluorescence confirming the lysosome stability of A549 cells in the process. Upon MUS 5 incubation, the LysoTracker channel images showed the time-dependent drop of intracellular red fluorescence in 1 h, implying the emerging of LMP. Meanwhile the ratiometric images of pH$_i$ showed the time-dependent enhancement of I_{int}/I_{agg} ratio infering pH$_i$ was decreased from ~5.70 to ~5.60 upon MUS 5 incubation in 1 h (Figure 7(j)). The dropping temporal profiles of LysoTracker fluorescence and pH$_i$ confirmed the distinct synchronization of cellular acidification to LMP induced by crystalline silica exposure. This implied the internalized particle-induced cellular acidification was triggered by MUS 5-induced LMP. This observation was also consistent with the previous reports that the leakage of acidic lysosomal enzymes (e.g., cathepsins and acidic sphingomyelinases) was one of the origins for the silica-induced cell death [50].

4 Conclusions

Taken together, three BODIPY derivatives were shown to present a pH-activated transition between AIE and intrinsic emission. The ratiometric pH sensing capacity of these compounds was achieved via a dual excitation/dual emission mode, with **BBI-3** displaying still the ratiometric pH sensing ability with a dual emission mode. The different pK_a values of the three compounds suggested that modifying benzimidazole moiety with different substituents offers a reliable strategy to regulate their functional pH range. In addition, **BBI-1** was applied for ratiometric pH$_i$ imaging in A549 cells, and the small particle-induced cellular acidification was found to be closely associated with particle size and chemical nature of the particle. Synchronization of lysosome disruption with cellular acidification in the crystalline silica-induced silicosis was observed directly by co-staining A549 cells with LysoTracker and **BBI-1**. Therefore, **BBI-1** could potentially act as a theranostic agent for the study of cellular acidification-related diseases. This article provided also a useful example for the design of ratiometric sensors by modifying fluorophore to possess an adjustable AIE/intrinsic emission transition.

Acknowledgements This work was supported by the National Basic Research Program of China (2015CB856300), the National Natural Science Foundation of China (21571099, 21731004) and the Natural Science Foundation of Jiangsu Province (BK20150054).

Conflict of interest The authors declare that they have no conflict of interest.

Supporting information The supporting information is available online at http://chem.scichina.com and http://link.springer.com/journal/11426. The supporting materials are published as submitted, without typesetting or editing. The responsibility for scientific accuracy and content remains entirely with the authors.

1 Stern ST, Adiseshaiah PP, Crist RM. *Part Fibre Toxicol*, 2012, 9: 20
2 Thibodeau MS, Giardina C, Knecht DA, Helble J, Hubbard AK. *Toxicol Sci*, 2004, 80: 34–48
3 Wan Q, Chen S, Shi W, Li L, Ma H. *Angew Chem Int Ed*, 2014, 53: 10916–10920
4 Wang X, Meier RJ, Wolfbeis OS. *Angew Chem Int Ed*, 2013, 52: 406–409
5 Tantama M, Hung YP, Yellen G. *J Am Chem Soc*, 2011, 133: 10034–10037
6 Chen Y, Zhu C, Cen J, Bai Y, He W, Guo Z. *Chem Sci*, 2015, 6: 3187–3194
7 Casey JR, Grinstein S, Orlowski J. *Nat Rev Mol Cell Biol*, 2010, 11: 50–61
8 Chrétien D, Bénit P, Ha HH, Keipert S, El-Khoury R, Chang YT, Jastroch M, Jacobs HT, Rustin P, Rak M. *PLoS Biol*, 2018, 16: e2003992
9 Zhang J, Wei H, Tan J, Qiao W, Guan Y, Zhang J. *Sci China Chem*, 2018, 61: 328–335
10 Hong Y, Lam JWY, Tang BZ. *Chem Soc Rev*, 2011, 40: 5361
11 Mei J, Leung NLC, Kwok RTK, Lam JWY, Tang BZ. *Chem Rev*, 2015, 115: 11718–11940
12 Yu CYY, Xu H, Ji S, Kwok RTK, Lam JWY, Li X, Krishnan S, Ding D, Tang BZ. *Adv Mater*, 2017, 29: 1606167
13 Li Q, Li Z. *Sci China Chem*, 2015, 58: 1800–1809
14 Chen S, Hong Y, Liu Y, Liu J, Leung CWT, Li M, Kwok RTK, Zhao E, Lam JWY, Yu Y, Tang BZ. *J Am Chem Soc*, 2013, 135: 4926–4929
15 Qin AJ, Zhang Y, Han N, Mei J, Sun JZ, Fan WM, Tang BZ. *Sci China Chem*, 2012, 55: 772–778
16 Wang ZT, Fang Y, Sun JZ, Qin AJ, Tang BZ. *Sci China Chem*, 2013, 56: 1187–1190
17 Sun YQ, Liu J, Zhang H, Huo Y, Lv X, Shi Y, Guo W. *J Am Chem Soc*, 2014, 136: 12520–12523
18 Kim S, Tachikawa T, Fujitsuka M, Majima T. *J Am Chem Soc*, 2014, 136: 11707–11715
19 Qin W, Baruah M, De Borggraeve WM, Boens N. *J Photochem Photobiol A-Chem*, 2006, 183: 190–197
20 Kolemen S, Işık M, Kim GM, Kim D, Geng H, Buyuktemiz M, Karatas T, Zhang XF, Dede Y, Yoon J, Akkaya EU. *Angew Chem Int Ed*, 2015, 54: 5340–5344
21 Pettit GR, Thornhill AJ, Moser BR, Hogan F. *J Nat Prod*, 2008, 71: 1561–1563
22 Ottenwaelder X, Ruiz-García R, Blondin G, Carasco R, Cano J, Lexa D, Journaux Y, Aukauloo A. *Chem Commun*, 2004, 6: 504–505
23 Costantini LM, Gilberti RM, Knecht DA. *PLoS ONE*, 2011, 6: e14647
24 Kowada T, Maeda H, Kikuchi K. *Chem Soc Rev*, 2015, 44: 4953–4972
25 Daly B, Ling J, de Silva AP. *Chem Soc Rev*, 2015, 44: 4203–4211
26 Mukherjee S, Thilagar P. *Chem Eur J*, 2014, 46: 9052–9062
27 Zhu X, Liu R, Li Y, Huang H, Wang Q, Wang D, Zhu X, Liu S, Zhu H. *Chem Commun*, 2014, 50: 12951–12954
28 Li Z, Zheng M, Guan X, Xie Z, Huang Y, Jing X. *Nanoscale*, 2014, 6: 5662–5665
29 Kim HJ, Heo CH, Kim HM. *J Am Chem Soc*, 2013, 135: 17969–17977
30 Sevinç G, Küçüköz B, Yılmaz H, Şirikçi G, Yaglioglu HG, Hayvalı M, Elmali A. *Sensor Actuat B-Chem*, 2014, 193: 737–744
31 Li Z, Li LJ, Sun T, Liu L, Xie Z. *Dyes Pigments*, 2016, 128: 165–169
32 Dong Y, Lam JWY, Qin A, Li Z, Sun J, Sung HHY, Williams ID, Tang BZ. *Chem Commun*, 2007, 127: 40–42
33 Zhang Z, Xu B, Su J, Shen L, Xie Y, Tian H. *Angew Chem Int Ed*, 2011, 50: 11654–11657
34 Shen XY, Yuan WZ, Liu Y, Zhao Q, Lu P, Ma Y, Williams ID, Qin A, Sun JZ, Tang BZ. *J Phys Chem C*, 2012, 116: 10541–10547
35 Masuda A, Oyamada M, Nagaoka T, Tateishi N, Takamatsu T. *Brain Res*, 1998, 807: 70–77
36 Jaganathan H, Godin B. *Adv Drug Deliver Rev*, 2012, 64: 1800–1819
37 Ding M, Chen F, Shi X, Yucesoy B, Mossman B, Vallyathan V. *Int Immunopharmacol*, 2002, 2: 173–182
38 Hnizdo E. *Occupl Environ Med*, 2003, 60: 237–243
39 Greenberg MI, Waksman J, Curtis J. *Disease-a-Month*, 2007, 53: 394–416
40 Fubini B, Hubbard A. *Free Radical Biol Med*, 2003, 34: 1507–1516
41 Deshpande A, Narayanan PK, Lehnert BE. *Toxicol Sci*, 2002, 67: 275–283
42 Jessop F, Hamilton Jr RF, Rhoderick JF, Fletcher P, Holian A. *Toxicol Appl Pharmacol*, 2017, 318: 58–68
43 Huang DM, Hung Y, Ko BS, Hsu SC, Chen WH, Chien CL, Tsai CP, Kuo CT, Kang JC, Yang CS, Mou CY, Chen YC. *FASEB J*, 2005, 19: 2014–2016
44 Boya P, Kroemer G. *Oncogene*, 2008, 27: 6434–6451
45 Kroemer G, Jäättelä M. *Nat Rev Cancer*, 2005, 5: 886–897
46 Merget R, Bauer T, Küpper H, Philippou S, Bauer H, Breitstadt R, Bruening T. *Arch Toxicol*, 2002, 75: 625–634
47 Mossman BT, Churg A. *Am J Respir Crit Care Med*, 1998, 157: 1666–1680
48 Thibodeau M, Giardina C, Hubbard AK. *Toxicol Sci*, 2003, 76: 91–101
49 Sohaebuddin SK, Thevenot PT, Baker D, Eaton JW, Tang L. *Part Fibre Toxicol*, 2010, 7: 22
50 Yan X, Ye T, Hu X, Zhao P, Wang X. *Sci Rep*, 2016, 6: 27875